Available online at www.sciencedirect.com
ScienceDirect
Trans. Nonferrous Met. Soc. China 35(2025) 3902−3918
Transactions of Nonferrous Metals Society of China
www.tnmsc.cn

Collaborative optimization method for sintering schedule of ternary cathode materials under microscopic coupling constraints

Jia-yao CHEN[1], Ning CHEN[1], Hong-zhen LIU[1], Zheng-wei XU[2], Zhi-xing WANG[2], Wei-hua GUI[1], Wen-jie PENG[2]

1. School of Automation, Central South University, Changsha 410083, China;
2. School of Metallurgy and Environment, Central South University, Changsha 410083, China

Received 27 June 2024; accepted 24 March 2025

Abstract: A collaborative optimization method for the sintering schedule of ternary cathode materials was proposed under microscopic coupling constraints. An oxygen vacancy concentration prediction model based on microscopic thermodynamics and a growth kinetics model based on neural networks were established. Then, optimization formulations were constructed in three stages to obtain an optimal sintering schedule that minimized energy consumption for different requirements. Simulations demonstrate that the models accurately predict the oxygen vacancy concentrations and grain size, with root mean square errors of approximately 5% and 3%, respectively. Furthermore, the optimized sintering schedule not only meets the required quality standards but also reduces sintering time by 12.31% and keeping temperature by 11.96%. This research provides new insights and methods for the preparation of ternary cathode materials.

Key words: ternary cathode materials; microscopic thermodynamics; oxygen vacancy concentration; grain growth; sintering schedule optimization

1 Introduction

New energy vehicles play a crucial role in the global new energy industry [1,2]. Ternary cathode materials, as the core components of lithium-ion batteries in these vehicles, are essential for enhancing battery energy density and cycle stability [3,4]. However, the sealed preparation process hinders the monitoring of intermediate states, which are critical for ensuring product quality. Additionally, manually setting the sintering schedule is time-consuming and can lead to high energy consumption, resulting in low preparation efficiency. Therefore, in-depth research on the intermediate variables of ternary cathode materials and optimization of the sintering schedule is significant for improving preparation efficiency and reducing energy consumption.

Currently, much research focuses on predicting the performance indicators of the finished products, such as residual lithium, specific surface area, and particle size [5,6]. Among these, oxygen vacancy concentration and grain size are two key indicators that significantly affect electrical conductivity and chemical stability [7−10]. Existing studies have explored the relationship between oxygen vacancy concentration and Li-ion diffusion rate [11−13], as well as grain growth at various sintering temperatures and durations [14,15]. Mechanism models are frequently used to track grain evolution [16]; however, these approaches primarily depend on manual experimentation, and the impact of the sintering schedule on these processes has not been fully examined. Data-driven methods have become increasingly popular in material research for predicting

Corresponding author: Ning CHEN, Tel: +86-13875915950, E-mail: ningchen@csu.edu.cn
https://doi.org/10.1016/S1003-6326(25)66920-2

product microstructural performance [17−19], nano particle detection [20] and similar applications [21]. To track complex evolutionary processes, CHEN et al [22] proposed a multi-particle cellular automaton model and predicted the Li/Ni mixing parameters of the product. A multi-dimensional cellular automaton has also been established to describe the dynamic evolution of grain structures [23,24]. PINEAU et al [25] developed a three-dimensional cellular automaton method to simulate the dynamics of crystal faces, the formation of grooves at grain boundaries and the paired growth of grains. Nonetheless, these studies rarely consider an in-depth analysis of intermediate grain growth during the micro-reaction processes of ternary cathode materials.

The sintering schedule not only determines the microstructure and macroscopic performance of the material but also directly impacts the energy efficiency of the entire process. To achieve an optimal sintering schedule, it is essential to formulate an appropriate optimization framework based on key micro-performance indicators. Research on optimizing process parameters has been conducted in various industrial fields [26−28], including coke sintering [29], and aluminum part preparation [30], with the aim of enhancing product quality and production efficiency. TIWARI et al [31] identified optimal alloy process parameters targeting specific energy consumption, relative density, and surface roughness. While these studies primarily focus on macroscopic performance, microscopic indicators are equally vital, with some research delving into aspects such as porosity and micro-hardness [32]. In the case of ternary cathode materials, relevant research has not yet been explored in depth. The optimization of the sintering schedule should not only prioritize final product performance but also account for intermediate microscopic changes, considering both energy consumption and performance metrics. Therefore, it is crucial to develop a new perspective for constructing an optimization model that comprehensively integrates multiple factors.

To address the above issues, in this work, a collaborative optimization method for the sintering schedule of ternary cathode materials was proposed under microscopic coupling constraints. Then, a sintering schedule optimization method for ternary cathode materials is developed. Compared to our previous work [22], this study primarily focuses on segmenting the reactions during the heating stage and establishing a model for the microscopic particle evolution. This work laid the foundation for understanding the behavior of materials at different temperatures. However, it mainly focused on the heating stage and a few microscopic indicators, which were insufficient to guide the entire reaction process. Therefore, based on this, our study places greater emphasis on two key indicators: the oxygen vacancy concentration during the oxidation phase and the grain size during the temperature-keeping stage of ternary cathode materials, providing a more comprehensive description of the material evolution. Additionally, research on the development of sintering schedule is currently limited, leading to significant room for improvement in existing sintering plans. Existing studies generally fail to fully consider the impact of each reaction stage and its combined effect on sintering efficiency. Given that energy consumption is a critical factor in industrial processes, systematic analysis and discussion of sintering schedule optimization are conducted based on the models established. The method proposed in this study not only addresses the shortcomings of current sintering schedules but also provides new insights for future research in related fields. While optimizing the sintering process, this study is significant in improving material performance and reducing production costs, thus contributing to the practical application and sustainable development of ternary cathode materials. The main contributions of this work can be summarized as follows. (1) By combining experimental data with reaction mechanisms, the dynamic evolution of phase, structure, and morphology during the sintering process of ternary cathode materials is revealed. This differs from the study in Ref. [22], which primarily focuses on particle and structural variations. (2) This work proposes a thermodynamic-based prediction method for the oxygen vacancy concentration and a hybrid modeling approach that combines mechanism and data-driven methods for the grain growth process, capturing the structural and morphological evolution characteristics of the material. (3) A method for optimizing the sintering schedule with multiple indicators on a microcosmic scale is proposed, providing a scientific approach to achieving an energy-efficient sintering process that

meets product quality requirements.

2 Microscopic evolution mechanism of ternary cathode materials

In this section, the chemical reactions that occur during the primary sintering process of the nickel−cobalt−manganese (NCM) ternary cathode material $Ni_{0.83}Co_{0.11}Mn_{0.06}O_2$ (Ni83) are analyzed. Then, to obtain the two important parameters of oxygen vacancy concentration and grain size, the experimental designs for electron paramagnetic resonance (EPR) and scanning electron microscope (SEM) are introduced and analyzed in this section.

During the sintering process of NCM materials, the primary reaction involves two raw materials: the lithium source $LiOH·H_2O$ and the precursor $Ni_{0.83}Co_{0.11}Mn_{0.06}(OH)_2$. These two substances are mixed according to the stoichiometric ratio in the reaction equation and loaded into a saggar, and then sent into a roller kiln. The saggar is transported from the entrance to the exit of the roller kiln at a predetermined roller speed, undergoing complex physical and chemical reactions along the way. Ultimately, the final ternary cathode material product Ni83 is obtained. The main reaction equation during this process is as follows:

$$Ni_{0.83}Co_{0.11}Mn_{0.06}(OH)_2+LiOH\cdot H_2O+0.25O_2 \rightarrow LiNi_{0.83}Co_{0.11}Mn_{0.06}O_2+2.5H_2O \quad (1)$$

The two substances do not react immediately to form the final product during the sintering process. Instead, the microscopic evolution can be viewed as a series of multiple complex chemical reactions. According to the literature [22,33,34], the preparation process of NCM materials can be described in three stages, allowing a model to be established based on the characteristics of each stage. Therefore, the reaction can be divided into three main sub-reactions: thermal decomposition of $LiOH·H_2O$, thermal decomposition of the precursor, and oxidation reaction of the precursor, as illustrated in Eqs. (2)−(5):

$$LiOH\cdot H_2O \rightarrow LiOH+H_2O \quad (2)$$

$$Ni_xCo_yMn_{1-x-y}(OH)_2 \rightarrow Ni_xCo_yMn_{1-x-y}O+H_2O \quad (3)$$

$$LiOH \rightarrow 0.5Li_2O+0.5H_2O \quad (4)$$

$$Ni_xCo_yMn_{1-x-y}O+0.5\,Li_2O+0.25O_2 \rightarrow LiNi_xCo_yMn_{1-x-y}O_2 \quad (5)$$

To further clarify the reaction mechanisms, a relevant experimental scheme is designed. The precursor and $LiOH·H_2O$ are mixed and ground uniformly in a 1:1.05 ratio. They are then heated from room temperature to 800 °C in a tube furnace, and maintained at this temperature for 9 h, with samples taken at specific temperature intervals. Several samples with the nominal composition Ni83 can be obtained using the high-temperature solid-state method. During the heating stage, heating rates of 1.5 and 2 K/min are employed, with temperatures set at 400, 600, and 800 °C. For the temperature-keeping stage, keeping time of 3, 6, 9 h is selected, respectively. The obtained samples are collected and analyzed by EPR and SEM, as shown in Figs. 1−3.

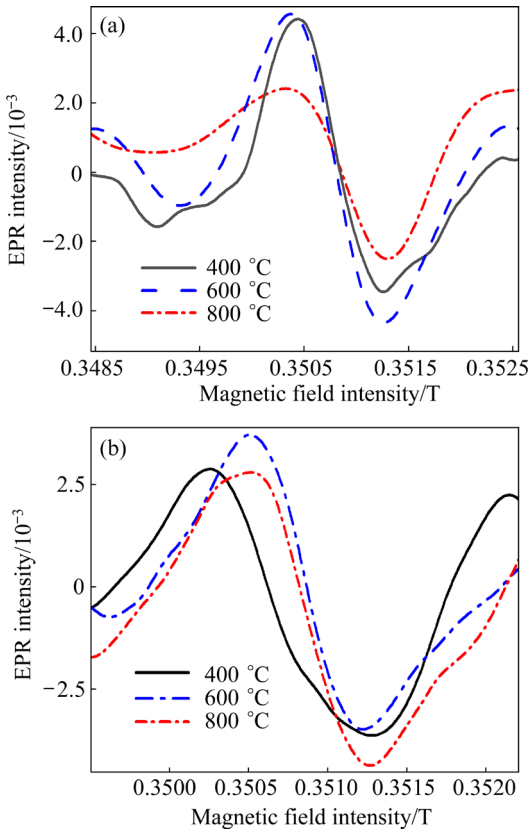

Fig. 1 EPR results at heating rates of 1.5 K/min (a) and 2 K/min (b)

EPR testing compares vacancy concentrations based on the different behaviors of defects in a magnetic field. The EPR results obtained from the experiment are presented in Fig. 1, where the horizontal axis represents the magnetic field intensity, and the peak value on the vertical axis indicates the level of vacancy concentration at the specific magnetic field intensity [35,36]. The EPR

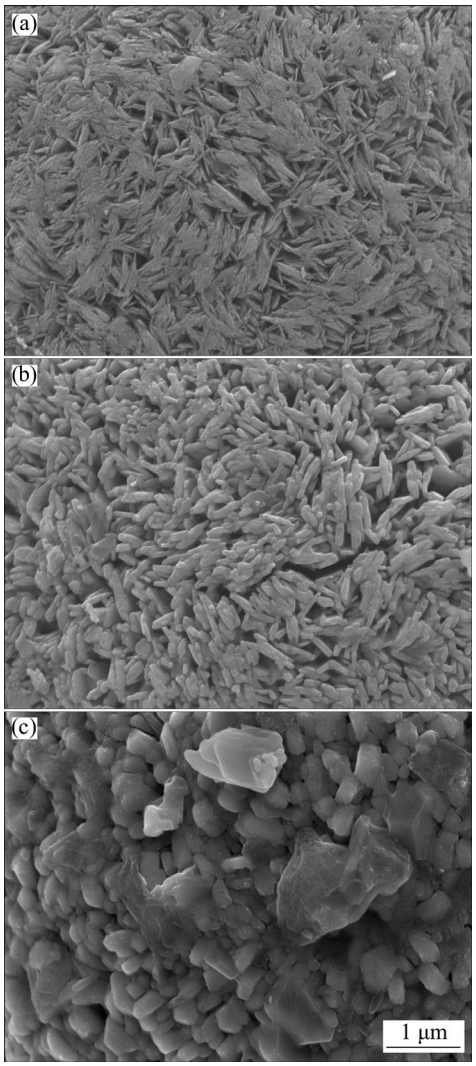

Fig. 2 SEM images during heating stage at 400 °C (a), 600 °C (b) and 800 °C (c)

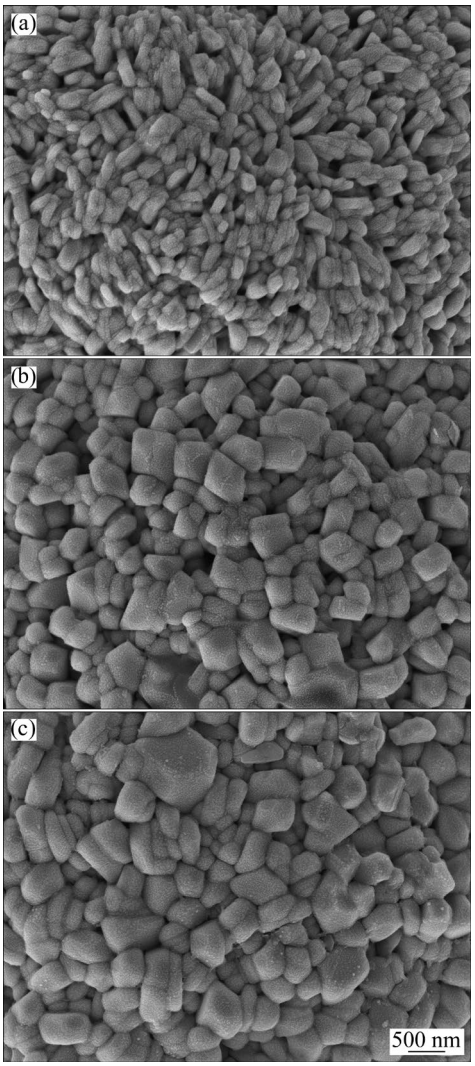

Fig. 3 SEM images during temperature-keeping stage for 3 h (a), 6 h (b) and 9 h (c)

experimental results illustrate the trend of oxygen vacancy concentration changes at various heating rates and sintering temperatures. As shown in Fig. 1, the oxygen vacancy concentration initially increases and then decreases as the temperature continues to rise, following the same variation pattern across different heating rates. At the same temperature, the oxygen vacancy concentration first decreases and then increases with the rising heating rate. To quantitatively describe these changes in oxygen vacancy concentration, we define the peak value of the EPR results as the oxygen vacancy concentration value. By normalizing the peak values of all EPR experimental results [37], we obtain the relative oxygen vacancy concentration, which serves as the output of the predictive model established in this work.

As shown in Fig. 2, during the grain growth process in the heating stage, various physical and chemical reactions lead to significant changes in grain morphology as the temperature increases. The shape of primary particles transitions from flaky to brick-like, and ultimately to rice-like, with particles adhering to one another, making it difficult to measure the grain size. In Fig. 3, during the temperature-keeping stage, the grains continue to grow significantly over several hours of constant temperature, resulting in noticeable changes in grain size. The grain boundaries between particles become distinct, and the grains are well-defined, ultimately achieving the size required for the final product.

From the above analysis, it is clear that the changes in oxygen vacancy concentration and grain

size are significant during the sintering process, and these indicators influence the performance of the product. Therefore, this study focuses on the evolution of grains throughout the sintering process by examining the oxygen vacancy concentration and grain size.

3 Prediction methods for key performance indicators of ternary cathode materials

During the sintering process, oxygen vacancy and grain size respectively reflect the structural and morphological characteristics of the material. In this section, the prediction methods for the key performance indicators of ternary cathode materials were proposed by conducting an in-depth analysis, with the aim of clarifying the microscopic changes in the sintering process.

3.1 Oxygen vacancy concentration prediction model for ternary cathode materials

From the analysis of the oxygen vacancy concentration, it is essential to consider comprehensive factors such as heating rate and sintering temperature in order to thoroughly understand and predict variations in oxygen vacancy concentration. According to Ref. [22], a cellular automaton during the sintering process can be established based on Arrhenius equations and the particles number set $\{N_{\mathrm{LiOH}}, N_{\mathrm{Li_2O}}, N_{\mathrm{NiCoMnO}}, N_{\mathrm{LiNiCoMnO_2}}, N_{\mathrm{H_2O}}\}$ can be obtained. Then, the relationship among oxygen vacancy concentration δ, heating rate β, sintering temperature T, and oxidation progress α can be described as follows:

$$\delta = f(\beta,\ T,\ \alpha) \tag{6}$$

where α is the progress of the oxidation reaction, which is the ratio of product particle number $N_{\mathrm{LiNiCoMnO_2}}$ to the initial precursor particle number N_{NiCoMnO}.

Since the change in oxygen vacancy concentration pertains to microscopic structure, an empirical formulation for these changes is designed based on mechanistic analysis and corresponding experimental trends. The data indicate that the concentration of oxygen vacancies is influenced by temperature and heating rate as shown in Section 2. Furthermore, the oxidation reaction is also the important cause of oxygen vacancy formation, and its progress directly impacts the concentration of oxygen vacancies.

Based on experimental data and relevant mechanistic knowledge, a relationship equation linking the concentration of oxygen vacancies to these three variables has been constructed. To capture the variation characteristics of oxygen vacancy concentration, a multi-exponential weighted fusion function is employed. Due to the complex variation trend of oxygen vacancy concentration, multi-exponential functions effectively capture these intricate data trends and changes by combining several exponential terms, making them more suitable for describing the fluctuations in oxygen vacancy concentration. Then, the influence of each factor on oxygen vacancy concentration is described as

$$f_i(x)=a_{3i-2}\cdot\exp\left(\frac{(x-a_{3i-1})^2}{-2a_{3i}^2}\right)\ (i=1,\ 2,\ 3) \tag{7}$$

where f_1, f_2 and f_3 correspond to the effects of β, T, and α, respectively. Here, the generic variable x in Eq. (7) represents β, T and α for $i=1$, 2, 3, respectively.

By considering the expressions of individual effects along with their interactions, a multi-exponential weighted fusion model can be obtained as

$$\begin{aligned}\delta(\beta,T,\alpha) &= f_1(\beta)+f_2(T)+f_3(\alpha)= \\ &a_1\cdot\exp\left(-\frac{(\beta-a_2)^2}{a_3^2}\right)+a_4\cdot\exp\left(-\frac{(T-a_5)^2}{a_6^2}\right)+ \\ &a_7\cdot\exp\left(-\frac{(\alpha-a_8)^2}{a_9^2}\right)\end{aligned} \tag{8}$$

where a_1, a_2, a_3, a_4, a_5, a_6, a_7, a_8, a_9 are model parameters.

The nonlinear least squares method is adopted to accurately estimate these model parameters. This method offers several advantages that make it widely applicable in data fitting and model development. Firstly, it is highly flexible and capable of handling various types of nonlinear models, making it suitable for complex functional relationships and effectively capturing intricate data trends. Secondly, by minimizing the sum of squared residuals between actual observations and model predictions, it provides high precision in parameter estimation, especially for data with strong nonlinear characteristics.

By minimizing the sum of squared errors (SSE) between the observed values and the model-

predicted values, the optimal model parameters can be found as

$$e_{\mathrm{SS1}}=\sum_{i=1}^{n_{\mathrm{ovc}}}\left[Y_i-\delta(\beta_i,\ T_i,\ \alpha_i)\right]^2 \tag{9}$$

where e_{SS1} represents SSE for oxygen vacancy concentration, n_{ovc} is the total number of samples, Y_i is the actual oxygen vacancy concentration for the ith sample, and $\delta(\beta_i, T_i, \alpha_i)$ represents the corresponding predicted value.

Then, the gradient descent method is used to update the parameters. By calculating the partial derivatives of SSE with respect to each parameter, new parameters can be obtained until the results converge, as shown in Eq. (10).

$$a_j^{\mathrm{new}}=a_j^{\mathrm{old}}-\eta\frac{\partial e_{\mathrm{SS1}}}{\partial a_j} \tag{10}$$

where a_j (j = 1, 2, ⋯⋯, 9) represents the jth model parameter, and η is the learning rate, which determines the step size of the parameter updates.

In this way, the oxygen vacancy concentration under different sintering conditions can be predicted. This allows us to precisely describe the variation in oxygen vacancy concentration during the heating stage. Through deeply analyzing the variation patterns of oxygen vacancy concentration in the sintering process, we can uncover the structural changes caused by the complex physicochemical behaviors of the material at high temperatures.

3.2 Grain growth process model of ternary cathode materials

The prediction model for grain growth process can be divided into heating stage and temperature-keeping stage. In the heating stage, several steps of thermal decomposition reactions occur, followed by the formation reactions of cathode materials, which are accompanied by significant morphological changes. The development direction of these reactions and the resulting structural changes directly determine the state and stability of grain growth.

During the heating phase of sintering, the material undergoes a transition from powder to consolidated body. This phase often involves the grain formation behavior that is frequently overlooked. As the basic stage of grain growth, it has an impact on the final product size. The prediction of initial grain size provides us with a starting point that allows us to more accurately predict and control grain growth at the temperature-keeping stage, which is critical for optimizing the microstructure and final performance of the material. However, the mechanism analysis and modeling of the grain growth process during the heating stage are challenging. Therefore, a data-driven model is adopted to predict the grain size at the heating stage in order to better understand and control the grain growth behavior during the entire sintering process.

On this basis, the grain size during the temperature-keeping stage can be predicted, covering the entire process from the beginning to the end of that stage, ensuring a comprehensive study of the grain size of the sintered samples. Through this method, a complete picture of the changes in grain size from start to end of sintering can be provided.

To reveal the nonlinear and complex relationship between particle size and sintering parameters, a neural network-based prediction model is established for the particle size at the end of the heating stage. The activation function for the input layer and the hidden layer is chosen as the tanh function, and the activation function for the output layer is chosen as the sigmoid function. The neural network structure is shown as Fig. 4.

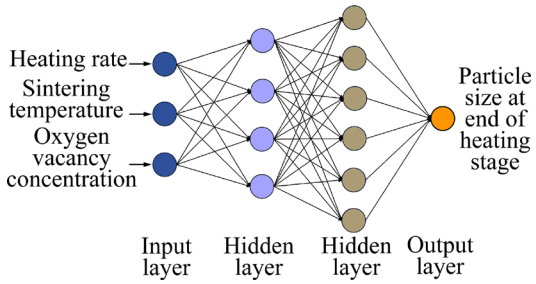

Fig. 4 Neural network structure diagram

The particle size at the end of the heating stage can be described as follows:

$$D_0=f_{\mathrm{out}}\left(\sum_{j=1}^{n_{\mathrm{h}}}(w_j y_j+b_{\mathrm{out}})\right) \tag{11}$$

where y_j is the output value of the jth neuron in the second hidden layer, and D_0 is the output value, which is the grain size at end of the heating stage. f_{out} is the activation function, w_j is the weight between the jth neuron of the hidden layer and the output layer, b_{out} is the biases of output layer, and n_{h} is the number of neurons in the second hidden layer.

The grain size model during the temperature-keeping stage mainly covers the entire process from the beginning of the temperature-keeping stage to the end of sintering. However, to enable effective evolution, the model lacks an initial grain size at the start of the temperature-keeping stage. If a random grain size is assumed, it may lead to inaccuracy in the final sintered grain size. Therefore, it is essential to predict the grain size at the end of the heating stage to ensure the accuracy and reliability of the model.

During the temperature-keeping stage, the grain growth process tends to stabilize due to the absence of complex chemical reactions. The key factors influencing this process include the keeping temperature and keeping time. According to Refs. [38−40], the Sellars−Anelli grain growth kinetics model is selected to predict grain size, as shown in Eq. (12).

$$D_t^n - D_0^n = At^m \exp\left(-\frac{Q}{RT}\right) \tag{12}$$

where D_t represents the average grain size at time t, Q is the activation energy for grain growth, A is the pre-exponential factor, R is the molar gas constant, and n and m are exponents.

To determine the unknown parameters n, A, m and Q, Eq. (12) can be transformed to Eq. (13) as

$$\ln(D_t^n - D_0^n) = \ln A + m\ln t - \frac{Q}{RT} \tag{13}$$

When solving for the unknown parameters in the model, the range of the grain growth exponent (n) needs to be determined. By substituting the n value into the equation and performing multiple trials, the values of A, m, Q and their errors can be calculated using experimental data.

Then, when the keeping time (t) is determined, the keeping time is a constant. Taking the partial derivative of Eq. (13) with respect to the keeping temperature $1/T$, the functional relationship $\ln(D_t^n - D_0^n)$ between and $1/T$ can be obtained as

$$Q = -R\frac{\partial \ln(D_t^n - D_0^n)}{\partial(1/T)} = -Rl \tag{14}$$

The parameters can be identified and the relationship curve between $\ln(D_t^n - D_0^n)$ and $1/T$ can be obtained. The average slope of this curve is denoted as l.

Similarly, when the keeping temperature T is determined, let the keeping temperature be a constant. The average slope of the relationship between $\ln(D_t^n - D_0^n)$ and $1/T$ is denoted as m, as shown in Eq. (15).

$$m = -R\frac{\partial \ln(D_t^n - D_0^n)}{\partial(\ln t)} \tag{15}$$

For the grain growth exponent n, the Levenberg−Marquardt (LM) algorithm is used for identification. The SSE is taken as a function of n, and the regression sum of squared errors is used as the optimization objective to obtain the optimal n value. The error formulation is introduced as shown in Eq. (16). The LM algorithm is particularly advantageous for this application because it efficiently handles the non-linear nature of the grain growth model, providing faster convergence to the optimal solution compared to traditional methods. Additionally, its combination of gradient and second-order information ensures stability and robustness in parameter estimation, making it well-suited for accurately identifying the grain growth exponent in complex systems.

$$e_{SS2} = \sum_{i=1}^{n_{gs}} (D_{pred,i} - D_{exp,i})^2 \tag{16}$$

where e_{SS2} represents SSE for grain size, n_{gs} is the total number of samples, $D_{pred,i}$ is the predicted grain size for the ith sample, and $D_{exp,i}$ the corresponding actual value.

4 Collaborative optimization of sintering schedule constrained by microscopic multi-reactant phase structure mechanism

In the preparation of ternary cathode materials, product quality and energy consumption are the most critical indicators, as determined by the sintering schedule. Therefore, it is necessary to formulate an appropriate sintering schedule to ensure efficiency and energy savings in the roller kiln. According to the mechanism analysis of the reactions, the optimization of the sintering process can be divided into three main stages: thermal decomposition, oxidation, and grain growth. Correspondingly, indicators in each stage can be selected as loss on ignition (LOI), oxygen vacancy concentration (OVC), and grain size (GS), as shown in Fig. 5.

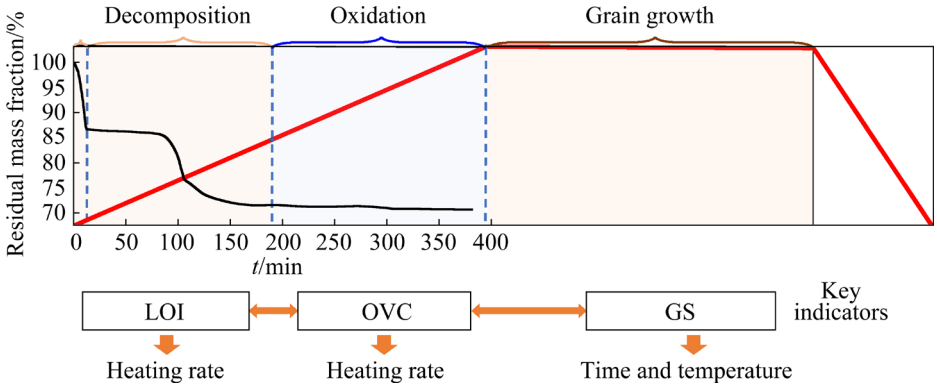

Fig. 5 Implementation concept of sintering schedule optimization

Based on the above established models, the variations in the three key indicators under different sintering schedules can be obtained. To achieve energy efficiency, the goal of sintering schedule collaborative optimization is to obtain the fastest sintering schedule while ensuring that all key performance indicators are within the acceptable range. The three elements that determine the sintering system are heating rate, keeping temperature, and keeping time, with different elements requiring optimization at each stage. The specific optimization formulations at each stage can be described as follows.

(1) Optimization of thermal decomposition stage

The thermal decomposition reaction stage mainly includes the thermal decomposition of $LiOH·H_2O$ and the precursor. The primary objective of the thermal decomposition stage is to remove the moisture from the raw materials completely. If the thermal decomposition time is too short, the moisture in the raw materials will not be fully removed, preventing subsequent oxidation reactions and grain growth stages from occurring. Conversely, if the sintering temperature is too high, the energy consumption required for sintering will increase, and preparation costs will rise substantially. Therefore, the LOI is selected to reflect the moisture content in the material, which is defined as the degree of dehydration occurring during the reaction process. According to Ref. [22], LOI is related to both the heating rate and the reaction time in the sintering schedule. The main objective of optimization in the thermal decomposition stage is to obtain an optimal heating rate that minimizes the decomposition time before the oxidation reaction begins, while meeting the LOI requirements, as shown in Eq. (17).

$$\begin{aligned}&\min J_1 = t_{\mathrm{w}}\\ &\text{s.t.}\begin{cases} W_{\mathrm{loss}} = f_{\mathrm{ts}}(\beta_1, t)\\ t = T/\beta_1\\ t_{\mathrm{w}} = T_{\mathrm{te}}/\beta_1\\ \beta_{\min} \le \beta_1 \le \beta_{\max}\\ t_{\min} \le t \le t_{\max}\\ t_{\mathrm{w,min}} \le t_{\mathrm{w}} \le t_{\mathrm{w,max}}\\ W_{\mathrm{ideal}} - \Delta W \le W_{\mathrm{loss}}(t_{\mathrm{w}}) \le W_{\mathrm{ideal}} + \Delta W \end{cases}\end{aligned} \tag{17}$$

where J_1 is the objective function to be minimized, representing the total thermal decomposition time t_{w}. t is the current sintering time, and β_1 is the heating rate at the current stage. W_{loss} represents the LOI at current t and β_1, calculated by the prediction model f_{ts} described in Ref. [22]. T is the current sintering temperature and T_{te} is the sintering temperature at the completion of the thermal decomposition reaction. $\beta_{\min}$ and $\beta_{\max}$ are bounds for the heating rate. $t_{\min}$ and $t_{\max}$ are time limits for current stage. $t_{\mathrm{w,min}}$ and $t_{\mathrm{w,max}}$ are bounds for total time. W_{ideal} denotes the ideal LOI, and ΔW represents the allowable fluctuation tolerance of LOI.

(2) Optimization of oxidation stage

The oxidation reaction stage mainly includes the oxidation reaction of nickel in the precursor, and oxygen vacancy in the material is a key indicator. The oxygen vacancy concentration is generally adjusted to meet the requirements of electrochemical performance, and it varies within a certain range. Based on the microscopic mechanism, the OVC is related to the oxidation reaction progress, heating rate, and sintering temperature.

The main objective of optimization in the oxidation stage is to obtain an optimal heating rate that minimizes the oxidation time, meeting the OVC requirements, as shown in Eq. (18).

$$\min J_2=t_{\mathrm{d}}$$
$$\text{s.t.}\begin{cases} W_{\mathrm{vacancy}}=f_{\mathrm{yh}}(\beta_2,T,\alpha) \\ t=(T-T_{\mathrm{ys}})/\beta_2 \\ t_{\mathrm{d}}=(T_{\mathrm{ye}}-T_{\mathrm{ys}})/\beta_2 \\ \beta_{\min}\le\beta_2\le\beta_{\max} \\ t_{\min}\le t\le t_{\max} \\ t_{\mathrm{d,min}}\le t_{\mathrm{d}}\le t_{\mathrm{d,max}} \\ W_{\mathrm{v,min}}\le W_{\mathrm{vacancy}}(t_{\mathrm{d}})\le W_{\mathrm{v,max}} \end{cases} \tag{18}$$

where J_2 is the objective function to be minimized, representing the total duration of the oxidation stage t_{d}. β_2 is the heating rate during this stage. W_{vacancy} denotes the oxygen vacancy concentration calculated by the prediction model f_{yh} described in Eq. (8). T_{ys} and T_{ye} represent the starting and ending temperatures of the oxidation stage, respectively. $t_{\mathrm{d,min}}$ and $t_{\mathrm{d,max}}$ are the bounds for the total duration. $W_{\mathrm{v,min}}$ and $W_{\mathrm{v,max}}$ are the allowable limits for the final oxygen vacancy concentration.

(3) Optimization of grain growth stage

Grain growth is the process by which the GS of a material continuously increases under the influence of heat. The GS is closely related to the keeping-time and keeping-temperature. A longer keeping-time or a higher keeping-temperature may lead to the larger GS. However, if the temperature is too low or the time is insufficient, it may result in incomplete grain growth. Excessively high temperatures increase the risk of cation mixing and microcrack formation and result in high energy consumption.

In addition, the primary particles mainly guide optimization, and the prediction model accuracy is also for the primary particles. On the one hand, they play a crucial role in determining the electrochemical performance of the material. On the other hand, as the fundamental building blocks of the material, the physicochemical performance of primary particles may influence the formation and behavior of secondary particles.

However, it does not imply that only a single indicator can be used for optimization. To achieve a better sintering schedule, a combination of multiple indicators can be employed in the optimization. Considering various indicators will provide a more comprehensive evaluation of different aspects of the sintering process, leading to better overall results. The optimization method proposed aims to effectively integrate these indicators to enhance the overall performance of the sintering schedule.

The main objective of optimization in the grain growth stage is to obtain the minimum time and lowest temperature that meet the grain size requirement, as shown in Eq. (19).

$$\min J_3=w_1t_{\mathrm{b}}+w_2T_{\mathrm{bw}}$$
$$\text{s.t.}\begin{cases} D_{\mathrm{bw}}=f_{\mathrm{bw}}(t,T_{\mathrm{bw}},D_0) \\ t_{\mathrm{b,min}}\le t_{\mathrm{b}}\le t_{\mathrm{b,max}} \\ T_{\mathrm{bw,min}}\le T_{\mathrm{bw}}\le T_{\mathrm{bw,max}} \\ \beta_1t_{\mathrm{w}}+\beta_2t_{\mathrm{d}}\le T_{\mathrm{bw}} \\ D_{\mathrm{bw,min}}\le D_{\mathrm{bw}}(t_{\mathrm{b}},T_{\mathrm{bw}})\le D_{\mathrm{bw,max}} \end{cases} \tag{19}$$

where J_3 is the objective function to be minimized. w_1 and w_2 are the weighting coefficients for time and temperature, respectively. t_{b} represents the grain growth time, and T_{bw} is the grain growth keeping temperature. D_{bw} is the grain size calculated by the prediction model f_{bw} described in Eq. (12). $t_{\mathrm{b,min}}$ and $t_{\mathrm{b,max}}$ are the bounds for the grain growth time. $T_{\mathrm{bw,min}}$ and $T_{\mathrm{bw,max}}$ are the limits for the sintering temperature. $D_{\mathrm{bw,min}}$ and $D_{\mathrm{bw,max}}$ represent the required range for the final grain size.

The optimization formulations described above involve optimizing the sintering schedule in three stages. These stages can be solved independently but are also interrelated. Summarizing the optimization processes for these three stages, the collaborative optimization formulation for the sintering schedule can be constructed, as shown in Fig. 6.

By solving the three optimization problems, the optimal heating rate, keeping time, and keeping-temperature can be obtained. These three elements will result in a sintering schedule with minimal energy consumption and optimal product quality.

5 Simulation results

The model parameters are determined using actual experimental data. The effectiveness of the proposed model is verified by simulating the oxygen vacancy and grain size under different sintering conditions. Subsequently, the optimal sintering schedules required for various requirements are

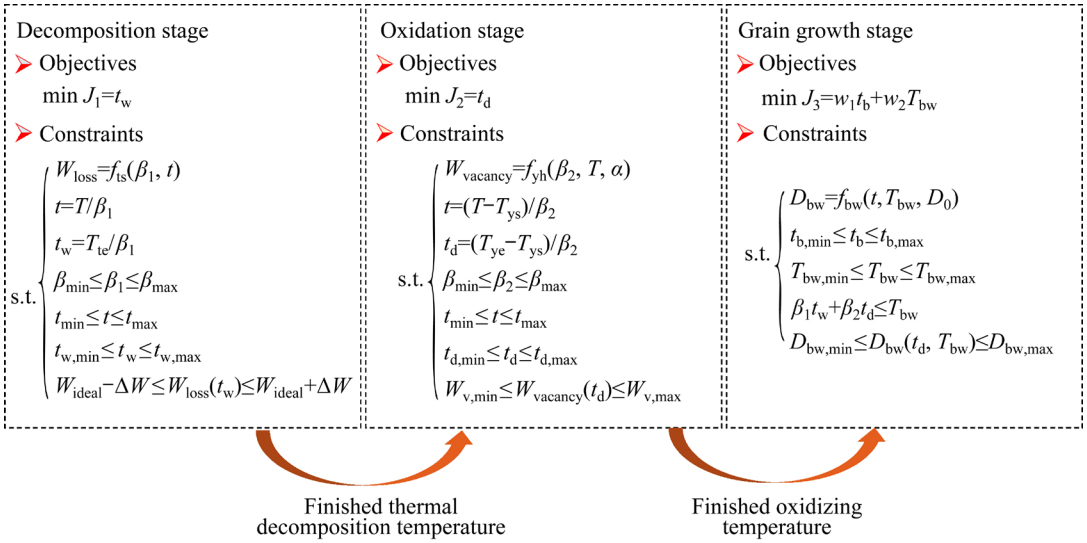

Fig. 6 Collaborative optimization formulation of sintering schedule

obtained using the proposed optimization method, and the feasibility of the optimization algorithm is validated with real data.

5.1 Oxygen vacancy concentration predictions

To verify the effectiveness of the oxygen vacancy concentration prediction model, the model parameters need to be determined first. Combining Eqs. (9) and (10) and actual sintering data, the parameters set for the oxygen vacancy prediction is obtained, as listed in Table 1.

Table 1 Parameters set for oxygen vacancy prediction

a_1	a_2	a_3	a_4	a_5	a_6	a_7	a_8	a_9
0.0048	1.5	1.2	0.0026	650	20	0.5	0.001	0.1

By inputting the corresponding heating rate, reaction temperature, and reaction progress data, the predicted oxygen vacancy concentrations under different conditions (1.5 and 2 K/min) are calculated. The comparison between the predicted and actual values of oxygen vacancy concentration at different heating rates is shown in Fig. 7.

The simulation results under different heating rates are evaluated using multiple metrics to assess the effect of the oxygen vacancy concentration model, including root mean square error (RMSE), coefficient of determination (R^2), and mean absolute error (MAE), as shown in Table 2.

The simulation results show that the trends of the simulated and actual oxygen vacancy concentrations are consistent, matching the actual variation trends

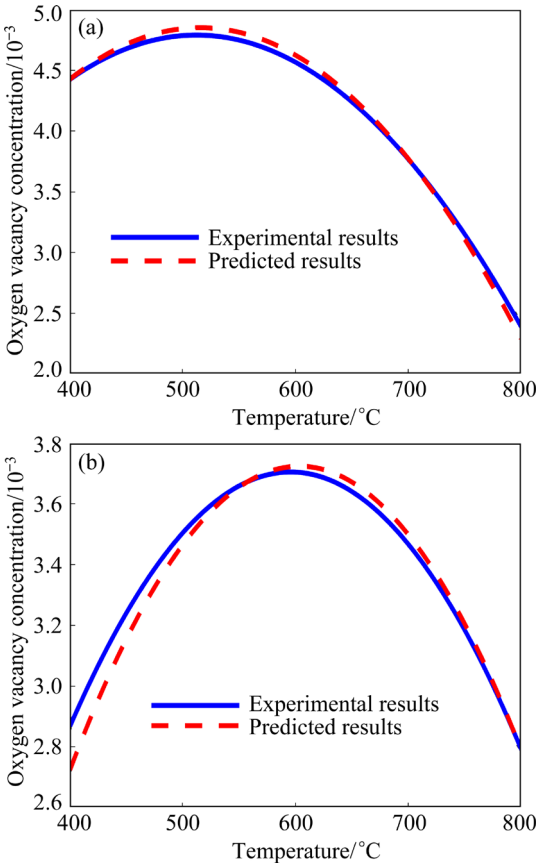

Fig. 7 Comparison of predicted and actual oxygen vacancy concentrations at heating rate of 1.5 K/min (a) and 2 K/min (b)

Table 2 Error analysis of predicted values

Heating rate/(K·min^{-1})	RMSE	R^2	MAE
1.5	0.0458	0.9742	0.1179
2	0.0527	0.9712	0.1235

of oxygen vacancy concentration. From the comparison between the simulation results and the actual values, the errors of the simulation results are within an acceptable range. The designed prediction model of oxygen vacancy concentration can dynamically simulate the changes in the oxygen vacancy structure of ternary cathode materials and can obtain real-time information on the material state changes within the roller kiln.

5.2 Grain size prediction

According to the mechanism analysis, the grain growth process is divided into two stages. In the heating stage, the parameters of neural network need to be determined first. The number of input layer nodes is set as 3, the number of output layer nodes is set as 1, and the number of hidden layer nodes is 10 with a 4×6 hidden layer network. The initial learning rate is set as 0.001 to ensure the stability and convergence speed of the training. A maximum of 20000 iterations is set to ensure sufficient training. The experimental data are split into a training set and a test set in a ratio of 8:2, ensuring the model learns from enough data while also evaluating its performance on an independent dataset. The model training stops when the MSE between the expected output and the model prediction is less than 0.0005. Using the experimental data from the heating stage under different sintering conditions and the neural network framework, the particle size at the end of the heating stage is predicted. The comparison between the model prediction and experimental results is shown in Fig. 8.

As shown in Fig. 8, under the influence of different factors, predicted values of the neural network for the particle size at the end of the heating stage overall show a consistent trend with the actual values. Relative error analysis of the predicted results indicates that the maximum relative error of the model is 1.4%, and the minimum relative error is 0.1%, demonstrating a high degree of fit between the neural network model and the data. Moreover, at the initial stage of training, the MSE decreases sharply. When the number of iterations reaches 4000, the MSE continues to decrease and stabilizes, achieving the required accuracy. Therefore, the experimental results indicate that the established neural network model can accurately predict the particle size during this stage.

Based on the neural network model, the particle size in the heating stage can be predicted, which can be used as the initial value for the grain growth process in the temperature-keeping stage. Using the temperature-keeping stage experimental data under different sintering conditions and the particle sizes from the heating stage, the values of A, m and Q can be obtained. Then, n=0.4908 is determined with a minimum sum of squared errors 0.03222. The parameters are listed in Table 3.

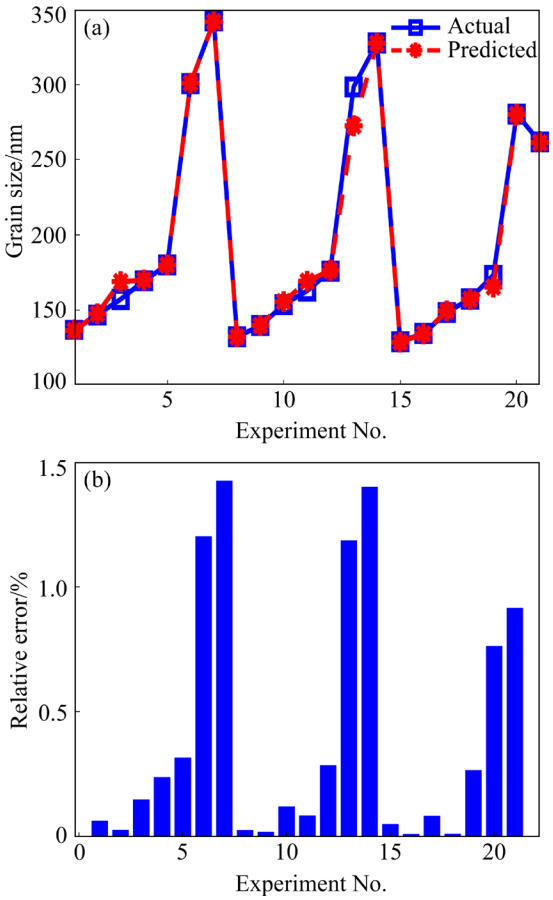

Fig. 8 Comparison of predicted and actual initial particle sizes (a), and their relative error (b)

Table 3 Parameter set for Sellars−Anelli kinetics model

n	Q/(kJ·mol^{-1})	m	A
0.4908	484.67	1.2942	64.3803

Therefore, the Sellars−Anelli kinetics model for the primary particle growth process of ternary cathode materials during the temperature-keeping stage can be obtained as follows.

$$D=\{D_0^{0.4908}+64.0383\cdot t^{1.2942}\cdot \exp[-484670/(RT)]\}^{1/0.4908} \quad (20)$$

Then, the primary particle size of ternary cathode materials during the temperature-keeping stage is predicted. The predictions are made at different keeping temperatures of 750 and 800 °C, under the condition of keeping for 9 h. The comparison between the mode predicted results and the actual experimental results is shown in Fig. 9.

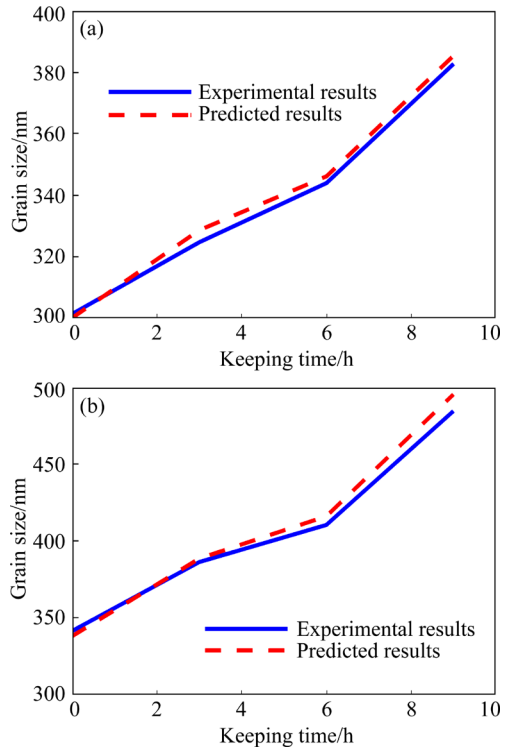

Fig. 9 Comparison of predicted and actual grain sizes during temperature-keeping stage at 750 °C (a) and 800 °C (b)

As shown in Fig. 9, the predicted results of the Sellars-Anelli model are consistent with the actual experimental results in terms of trends and values. The simulation results indicate that the established grain growth kinetics model can effectively reflect the grain growth characteristics of ternary cathode materials during the temperature-keeping stage, simulating the variation in grain size. This confirms the effectiveness and reliability of the model in grain size prediction.

5.3 Sintering schedule optimization

To verify the effectiveness of the proposed optimization methods, two conditions are designed based on different product requirements to optimize the sintering schedule. Under constraint condition I, the LOI is maintained within an error of 0.1%, the oxygen vacancy concentration is set between 0.001 and 0.0015, and the grain size is set between 420 and 440 nm. For the sintering schedule constraints, the heating rate is set to vary between 1 and 10 K/min, the platform temperature is set between 700 and 1000 °C, and the keeping time is set between 0 and 12 h. The sintering schedule is optimized according to constraint condition I, resulting in the optimization results shown in Table 4 and Fig. 10.

As shown in Table 4 and Fig. 10, the sintering schedule is optimized in three stages according to different production requirements. In the thermal decomposition stage, the heating rate is 2.428 K/min. In the oxidation stage, the heating rate is 2.9876 K/min, and heating continues at this rate until 704.2819 °C, followed by the temperature-keeping stage. After keeping at the temperature for 8.3703 h, the product achieves a LOI of 29.34%, an oxygen vacancy concentration of 0.0014, and a grain size of 436.8 nm, meeting the specified production requirements.

Under constraint condition II, with the LOI maintained within an error range of 0.3%, the oxygen vacancy concentration is set between 0.0015 and 0.002, and the grain size is set between 440 and 460 nm. The sintering schedule constraints are set the same as condition I. The sintering schedule is optimized according to constraint condition II, resulting in the optimization results shown in Table 5 and Fig. 11.

As shown in Table 5 and Fig. 11, the sintering schedule is optimized in three stages according to different production requirements. In the thermal decomposition stage, the heating rate is 2.431 K/min. In the oxidation stage, the heating rate is 2.7747 K/min, and heating continues at this rate until 703.0737 °C, followed by the temperature-keeping stage. After keeping at the temperature for 9.5424 h, the product achieves a LOI of 14.41%, an oxygen vacancy concentration of 0.0017, and a

Table 4 Optimization results for ternary cathode materials under constraint condition I

Decomposition heating rate/(K·min^{-1})	Decomposition end temperature/°C	Oxidation heating rate/(K·min^{-1})	Keeping temperature/°C	Keeping time/h
2.428	420.28	2.9876	704.2819	8.3703

Table 5 Optimization results for ternary cathode materials under constraint condition II

Decomposition heating rate/(K·min^{-1})	Decomposition end temperature/°C	Oxidation heating rate/(K·min^{-1})	Keeping temperature/°C	Keeping time/h
2.431	391.02	2.7747	703.0737	9.5424

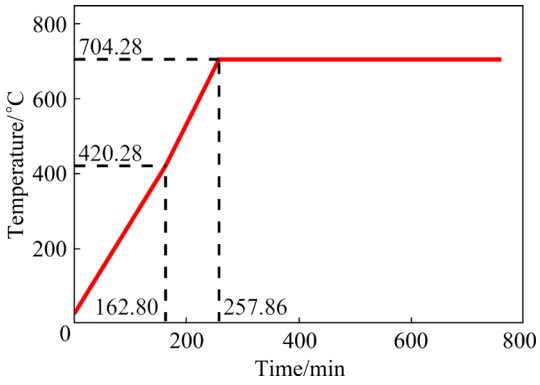

Fig. 10 Optimized sintering schedule under constraint condition I

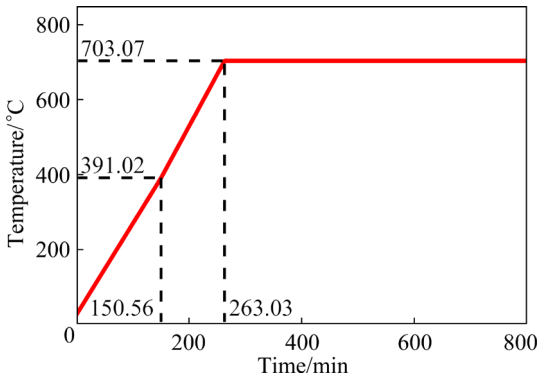

Fig. 11 Optimized sintering schedule under constraint condition II

grain size of 453.6 nm, meeting the specified production requirements.

Currently, there are methods such as co-precipitation, high-temperature solid-phase synthesis, and solvothermal synthesis for sintering Ni83 material [41]. Among them, the high-temperature solid-phase method is widely used in industrial production due to its simple preparation process and low cost, making it suitable for mass production. In terms of optimizing the sintering system for Ni83, there is currently no relevant research. Therefore, to demonstrate that the proposed optimization method can formulate a sintering schedule with minimal energy consumption that meets different production requirements, a comparative experiment on sintering energy consumption is designed. The sintering schedule optimization method proposed is compared to the existing general sintering method, which is denoted as the experimental group. The sintering schedule for the experimental group is set with a heating rate of 2 K/min, a keeping temperature of 800 °C, and a keeping time of 8 h. The optimized sintering schedule under constraint condition I is used as the control group for the comparative experiment. The comparison of the two sintering schedules is shown in Fig. 12.

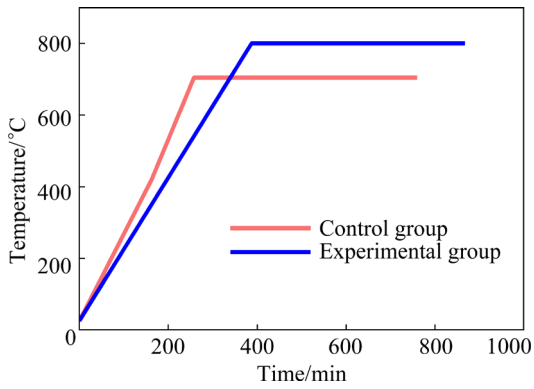

Fig. 12 Comparison of sintering schedules between experimental group and control group

Under the sintering schedule of the experimental group, the material achieves a LOI of 29.57%, an oxygen vacancy concentration of 0.0014, and a grain size of 436.7 nm, all within the performance indicator range specified in constraint condition I. The results show that both sintering schedules meet the given requirements. Under condition I, the heating rate is faster and the keep-temperature is lower, suggesting that sintering is more energy-efficient and the proposed method is effective. The material is sintered in a tube furnace using the sintering schedule from condition I, as shown in Fig. 13.

The sintering time for the two sintering schedules is calculated. Under the conditions that the performance indicators meet the constraint ranges, the sintering time for the experimental group is 867.5 min, with heating rate of 2 K/min, keeping temperature of 800 °C, and keeping time of 8 h. The sintering time for the control group obtained through the optimization model is 760.708 min, significantly shorter than that of the experimental group. This indicates that the

established optimization model is effective, capable of yielding the shortest sintering time and, consequently, the lowest energy consumption within the same performance indicator range.

Moreover, the proposed method has been used in the actual preparation of cathode material, as shown in Fig. 14. It effectively shortens the development cycle, improves the adaptability of sintering schedule to complex process requirements, and significantly reduces the energy consumption.

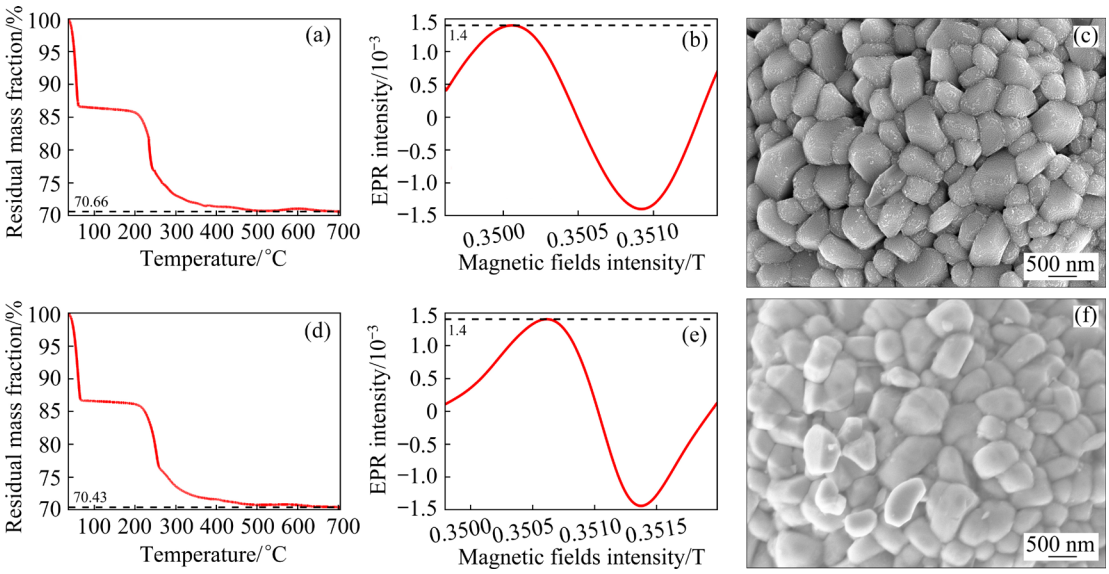

Fig. 13 TG curves (a, d), EPR curves (b, e) and SEM images (c, f) of materials sintered by optimized (a−c) and standard (d−f) schedule

Fig. 14 Actual application system interface

6 Conclusions

(1) The work focused on the preparation of Ni83 ternary cathode materials, proposing prediction models for oxygen vacancy concentration and grain size based on microscopic thermodynamics. It integrated chemical reaction mechanisms with experimental data to track grain structure evolution.

(2) The sintering schedule was optimized collaboratively in three stages, aiming to minimize reaction time at each stage while adhering to constraints for LOI, oxygen vacancy concentration, and grain size requirements.

(3) Simulation results demonstrated that the proposed optimization method could establish an efficient sintering schedule with minimal energy consumption, providing a theoretical framework that enhanced material development efficiency and supported sustainable material preparation.

CRediT authorship contribution statement

Jia-yao CHEN: Methodology, Validation, Writing – Original draft, Writing – Review & editing, Software, Data curation; **Ning CHEN:** Conceptualization, Supervision, Project administration, Methodology, Funding acquisition; **Hong-zhen LIU:** Software, Supervision, Methodology, Writing – Review & editing; **Zheng-wei XU:** Data curation, Formal analysis, Validation, Methodology; **Zhi-xing WANG:** Investigation, Supervision, Project administration; **Wei-hua GUI:** Investigation, Formal analysis, Supervision; **Wen-jie PENG:** Resources, Data curation, Supervision.

Declaration of competing interest

The authors declare that they have no known competing financial interests or personal relationships that could have appeared to influence the work reported in this paper.

Acknowledgments

This work was supported by the National Natural Science Foundation of China (No. 62033014), the Application Projects of Integrated Standardization and New Paradigm for Intelligent Manufacturing from the Ministry of Industry and Information Technology of China in 2016, and the Fundamental Research Funds for the Central Universities of Central South University, China (No. 2021zzts0700).

References

[1] ALSHARIF A, TAN C W, AYOP R, DOBI A, LAU K Y. A comprehensive review of energy management strategy in Vehicle-to-Grid technology integrated with renewable energy sources [J]. Sustainable Energy Technologies and Assessments, 2021, 47: 101439.

[2] SADEGHIAN O, OSHNOEI A, MOHAMMADI-IVATLOO B, VAHIDINASAB V, ANVARI-MOGHADDAM A. A comprehensive review on electric vehicles smart charging: Solutions, strategies, technologies, and challenges [J]. Journal of Energy Storage, 2022, 54: 105241.

[3] LU Shi-jie, LIU Yang, HE Zhen-jiang, LI Yun-jiao, ZHENG Jun-chao, MAO Jing, DAI Ke-hua. Synthesis and properties of single-crystal Ni-rich cathode materials in Li-ion batteries [J]. Transactions of Nonferrous Metals Society of China, 2021, 31(4): 1074−1086.

[4] CHANG Long-jiao, YANG Wei, CAI Ke-di, BI Xiao-long, WEI An-lu, YANG Rui-fen, LIU Jia-nan. A review on nickel-rich nickel-cobalt-manganese ternary cathode materials $LiNi_{0.6}Co_{0.2}Mn_{0.2}O_2$ for lithium-ion batteries: Performance enhancement by modification [J]. Materials Horizons, 2023, 10(11): 4776−4826.

[5] CHEN Jia-yao, GUI Wei-hua, DAI Jia-yang, YUAN Xiao-feng, CHEN Ning. An ensemble just-in-time learning soft-sensor model for residual lithium concentration prediction of ternary cathode materials [J]. Journal of Chemometrics, 2020, 34(5): e3225.

[6] CHEN Ning, XIE Mu-yan, CHEN Zhi-wen, JIANG Lu, LI Xu. Sintering process-monitoring method for ternary cathode materials based on recurrent variational autoencoder [J]. IEEE Transactions on Instrumentation and Measurement, 2023, 72: 1−13.

[7] SUN Cong-li, LIAO Xiao-bin, XIA Fan-jie, ZHAO Yan, ZHANG Lei, MU Sai, SHI Shan-shan, LI Yan-xi, PENG Hao-yang, van TENDELOO G, ZHAO Kang-ning, WU Jin-song. High-voltage cycling induced thermal vulnerability in $LiCoO_2$ cathode: Cation loss and oxygen release driven by oxygen vacancy migration [J]. ACS Nano, 2020, 14(5): 6181−6190.

[8] LUO Yu-hong, WEI Han-xin, TANG Lin-bo, WANG Zhen-yu, HE Zhen-jiang, YAN Cheng, MAO Jing, DAI Ke-hua, ZHENG Jun-chao. Nickel-rich and cobalt-free layered oxide cathode materials for lithium ion batteries [J]. Energy Storage Materials, 2022, 50: 274−307.

[9] NAGAUMI H, QIN Jian, YU Cheng-bin, WANG Xiao-guo, WANG Lin-sheng. Quantitative analysis of influence of α-Al(MnFeCr)Si dispersoids on hot deformation and microstructural evolution of Al−Mg−Si alloys [J]. Transactions of Nonferrous Metals Society of China, 2022, 32(6): 1805−1821.

[10] LIU Xin-rui, CHENG Jiao-yang, GUAN Yun-long, HUANG Song-tao, LIAN Fang. Oxygen vacancy in Li-rich Mn-based cathode materials: Origination, influence, regulation and characterization [J]. Materials Chemistry Frontiers, 2023, 7(17): 3434−3454.

[11] BI Yu-jing, YANG Wen-chao, DU Rui, ZHOU Jing-jing, LIU

Meng, LIU Yang, WANG De-yu. Correlation of oxygen non-stoichiometry to the instabilities and electrochemical performance of $LiNi_{0.8}Co_{0.1}Mn_{0.1}O_2$ utilized in lithium ion battery [J]. Journal of Power Sources, 2015, 283: 211−218.

[12] LI Qing-yu, YANG Guang-chang, CHU You-qi, TAN Chun-lei, PAN Qi-chang, ZHENG Feng-hua, LI Yu, HU Si-jiang, HUANG You-guo, WANG Hong-qiang. Enhanced electrochemical performance of Ni-rich cathode material by N-doped $LiAlO_2$ surface modification for lithium-ion batteries [J]. Electrochimica Acta, 2021, 372: 137882.

[13] XIAO Peng, LI Wen-hao, CHEN Shuai, LI Gang, DAI Zhong-jia, FENG Meng-dan, CHEN Xu, YANG Wen-sheng. Effects of oxygen pressurization on Li^+/Ni^{2+} cation mixing and the oxygen vacancies of $LiNi_{0.8}Co_{0.15}Al_{0.05}O_2$ cathode materials [J]. ACS Applied Materials & Interfaces, 2022, 14(28): 31851−31861.

[14] WANG Jie-xi, ZHANG Qiao-bao, LI Xin-hai, XU Da-guo, WANG Zhi-xing, GUO Hua-jun, ZHANG Kai-li. Three-dimensional hierarchical Co_3O_4/CuO nanowire heterostructure arrays on nickel foam for high-performance lithium ion batteries [J]. Nano Energy, 2014, 6: 19−26.

[15] XIA Yun-fei, NIE Min, WANG Zhen-bo, YU Fu-da, ZHANG Yin, ZHENG Li-li, WU Jin, KE Ke. Structural, morphological and electrochemical investigation of $LiNi_{0.6}Co_{0.2}Mn_{0.2}O_2$ cathode material synthesized in different sintering conditions [J]. Ceramics International, 2015, 41(9): 11815−11823.

[16] QIU Yi, LI Ying-ju, FENG Xiao-hui, ZHANG Ang, YANG Yuan-sheng. Numerical simulation of microstructure evolution in molten pool of nickel-based superalloy during selective laser melting [J]. Transactions of Nonferrous Metals Society of China, 2024, 34(2): 560−575.

[17] LING J L, HUTCHINSON M, ANTONO E, DECOST B, HOLM E A, MEREDIG B. Building data-driven models with microstructural images: Generalization and interpretability [J]. Materials Discovery, 2017, 10: 19−28.

[18] SEVERSON K A, ATTIA P M, JIN N, PERKINS N, JIANG B B, YANG Z, CHEN M, AYKOL M H, HERRING P K, FRAGGEDAKIS D, BAZANT M I, HARIS S J, CHUEH W C, BRAATZ R D. Data-driven prediction of battery cycle life before capacity degradation [J]. Nature Energy, 2019, 4(5): 383−391.

[19] CHEN Ning, DAI Jia-yang, TIAN Shuang, GUI Wei-hua. Data fusion based on-line product quality evaluation of ternary cathode material cyber-physical systems [J]. IET Cyber-Physical Systems: Theory & Applications, 2019, 4(4): 353−364.

[20] KHARIN A. Deep learning for scanning electron microscopy: Synthetic data for the nanoparticles detection [J]. Ultramicroscopy, 2020, 219: 113125.

[21] ZHOU Ping, GUO Dong-wei, CHAI Tian-you. Data-driven predictive control of molten iron quality in blast furnace ironmaking using multi-output LS-SVR based inverse system identification [J]. Neurocomputing, 2018, 308: 101−110.

[22] CHEN Ning, LIU Hong-jie, YANG Chun-hua, LIU Hong-zhen, CHEN Jia-yao, DAI Yuan-shen, YANG Peng, FENG Yue-xia, GUI Wei-hua, PENG Wen-jie, WANG Jie-xi. A multi-particle cellular automaton modeling method for grain dynamics evolution of nickel-rich cathode material [J]. Materials Today Energy, 2023: 35: 101291.

[23] LI Zhi-qiang, WANG Jun-sheng, HUANG Hou-bing. Grain boundary curvature based 2D cellular automata simulation of grain coarsening [J]. Journal of Alloys and Compounds, 2019, 791: 411−422.

[24] ADENSON M O, TEMPLETON C, BIERNACKI J J. Modeling pyrolysis-induced microstructural changes in biomass: A cellular automata approach [J]. Fuel, 2017, 210: 198−206.

[25] PINEAU A, GUILLEMOT G, REINHART G, REGULA G, MANGELINCK-NOËL N, GANDIN C A. Three-dimensional cellular automaton modeling of silicon crystallization with grains in twin relationships [J]. Acta Materialia, 2020, 191: 230−244.

[26] PENG Shi-tong, LI Tao, ZHAO Jia-li, LV Sheng-ping, TAN G, DONG Meng-meng, ZHANG Hong-chao. Towards energy and material efficient laser cladding process: Modeling and optimization using a hybrid TS-GEP algorithm and the NSGA-II [J]. Journal of Cleaner Production, 2019, 227: 58−69.

[27] LI Jing-chang, HU Jie-xiang, CAO Long-chao, WANG Sheng-yi, LIU Hua-ping, ZHOU Qi. Multi-objective process parameters optimization of SLM using the ensemble of metamodels [J]. Journal of Manufacturing Processes, 2021, 68: 198−209.

[28] YU Gang, CHAI Tian-you, LUO Xiao-chuan. Multiobjective production planning optimization using hybrid evolutionary algorithms for mineral processing [J]. IEEE Transactions on Evolutionary Computation, 2011, 15(4): 487−514.

[29] NATH N K, MITRA K. Mathematical modeling and optimization of two-layer sintering process for sinter quality and fuel efficiency using genetic algorithm [J]. Materials and Manufacturing Processes, 2005, 20(3): 335−349.

[30] PENG Tao, LV Jing-xiang, MAJEED A, LIANG Xi-hui. An experimental investigation on energy-effective additive manufacturing of aluminum parts via process parameter selection [J]. Journal of Cleaner Production, 2021, 279: 123609.

[31] TIWARI J, COZZOLINO E, DEVADULA S, ASTARITA A, KRISHNASWAMY H. Determination of process parameters for selective laser melting of inconel 718 alloy through evolutionary multi-objective optimization [J]. Materials and Manufacturing Processes, 2024, 39: 1019−1028.

[32] DELLA GATTA R, DEL SOL I D, CARAVIELLO A, ASTARITA A. Selective laser melting of an Al−Si−Mg−Cu alloy: Feasibility and processing aspects [J]. Materials and Manufacturing Processes, 2021, 36(12): 1438−1449.

[33] ZHANG Ming-jian, TENG Gao-feng, CHEN-WIEGART Y, DUAN Yan-dong, KO J, ZHENG Jia-xin, THIEME J, DOORYHEE E, CHEN Zong-hai, BAI Jian-ming, AMINE K, PAN Feng, WANG Feng. Cationic ordering coupled to reconstruction of basic building units during synthesis of high-Ni layered oxides [J]. Journal of the American Chemical Society, 2018, 140(39): 12484−12492.

[34] WU Ying-qiang, WU Han-feng, DENG Jiu-shuai, HAN Zhi-ding, XIAO Xiang, WANG Li, CHEN Zong-hai, DENG Yi-da, HE Xiang-ming. Insight of synthesis of single crystal

Ni-rich $LiNi_{1-x-y}Co_xMn_yO_2$ cathodes [J]. Advanced Energy Materials, 2024, 14(11): 2303758.

[35] FENG Li-wei, LIU Yang, WU Lei, QIN Wen-chao, YANG Zi-hao, LIU Jin-feng. Surface modification with oxygen vacancy in $LiNi_{0.5}Co_{0.2}Mn_{0.3}O_2$ for lithium-ion batteries [J]. Journal of Alloys and Compounds, 2021, 881: 160626.

[36] PENG Fan, ZHANG Li-xuan, YANG Guang-chang, LI Ya-hao, PAN Qi-chang, LI Yu, HU Si-jiang, ZHENG Feng-hua, WANG Hong-qiang, LI Qing-yu. Nanoscale surface modification to suppress capacity fade of Ni-rich layered oxide material at high cut-off voltage [J]. Chemical Engineering Journal, 2023, 451: 138911.

[37] YAO Liu, LI Yan-pei, GAO Xing-peng, CAI Ming-li, JIN Jun, YANG Jian-hua, XIU Tong-ping, SONG Zhen, BADDING M, WEN Zhao-yin. Microstructure boosting the cycling stability of $LiNi_{0.6}Co_{0.2}Mn_{0.2}O_2$ cathode through Zr-based dual modification [J]. Energy Storage Materials, 2021, 36: 179−185.

[38] DEVADAS C, SAMARASEKERA I V, HAWBOLT E B. The thermal and metallurgical state of steel strip during hot rolling: Part III. Microstructural evolution [J]. Metallurgical Transactions A, 1991, 22: 335−349.

[39] ANELLI E. Application of mathematical modelling to hot rolling and controlled cooling of wire rods and bars [J]. ISIJ International, 1992, 32(3): 440−449.

[40] STAKO R, ADRIAN H, ADRIAN A. Effect of nitrogen and vanadium on austenite grain growth kinetics of a low alloy steel [J]. Materials Characterization, 2006, 56(4/5): 340−347.

[41] NITTA N, YUSHIN G. High-capacity anode materials for lithium- ion batteries: Choice of elements and structures for active particles [J]. Particle & Particle Systems Characterization, 2014, 31(3): 317−336.

微观特征耦合约束下的三元正极材料烧结制度协同优化方法

陈嘉瑶[1]，陈 宁[1]，刘洪臻[1]，徐正伟[2]，王志兴[2]，桂卫华[1]，彭文杰[2]

1. 中南大学 自动化学院，长沙 410083；
2. 中南大学 冶金与环境学院，长沙 410083

摘 要：提出了微观特征耦合约束下三元正极材料烧结制度的协同优化方法，建立了基于微观热力学的氧空位浓度预测模型和基于神经网络的生长动力学模型，构建了三阶段优化问题，以获得在不同微观指标需求下最节能的烧结制度。仿真结果表明，所建立模型能够准确预测氧空位浓度和晶粒尺寸，均方根误差分别约为 5%和 3%。此外，优化后的烧结制度不仅满足所需的质量标准，还缩短了 12.31%的烧结时间，平台温度降低了 11.96%。该研究为三元正极材料的制备提供了新的视角和方法。

关键词：三元正极材料；微观动力学；氧空位浓度；晶粒生长；烧结制度优化

(Edited by Xiang-qun LI)